IEEE TRANSACTIONS ON
BIOMEDICAL
CIRCUITS AND SYSTEMS
A PUBLICATION OF THE IEEE CIRCUITS AND SYSTEMS SOCIETY
IEEE ENGINEERING IN MEDICINE AND BIOLOGY SOCIETY
Indexed in PubMed® and MEDLINE®, products of the United States National Library of Medicine

IEEE Xplore® Digital Library
http://ieeexplore.ieee.org/Xplore

A mm-Sized Wireless Implantable Device for Electrical Stimulation of Peripheral Nerves

Jayant Charthad, *Student Member, IEEE,* Ting Chia Chang, *Student Member, IEEE*, Zhaokai Liu, *Student Member, IEEE,* Ahmed Sawaby, *Student Member, IEEE*, Marcus J. Weber, *Student Member, IEEE,* Sam Baker, Felicity Gore, Stephen A. Felt, and Amin Arbabian, *Senior Member, IEEE*

***Abstract*—A wireless electrical stimulation implant for peripheral nerves, achieving >10× improvement over state-of-the-art in the depth/volume figure of merit (FOM), is presented. The fully integrated implant measures just 2 mm × 3 mm × 6.5 mm (39 mm^3, 78 mg), and operates at a large depth of 10.5 cm in a tissue phantom. The implant is powered using ultrasound and includes a miniaturized piezoelectric receiver (piezo), an IC designed in 180 nm HV BCD process, an off-chip energy storage capacitor, and platinum stimulation electrodes. The package also includes an optional blue light-emitting diode (LED) for potential applications in optogenetic stimulation in the future. A system-level design strategy for complete operation of the implant during the charging transient of the storage capacitor, as well as a unique downlink command/data transfer protocol, are presented. The implant enables externally programmable current-controlled stimulation of peripheral nerves, with a wide range of stimulation parameters, both for electrical (22 to 5,000 µA amplitude, ~14 to 470 µs pulse-width, 0 to 60 Hz repetition rate) and optical (up to 23 mW/mm^2 optical intensity) stimulation. Additionally, the implant achieves 15 V compliance voltage for chronic applications. Full integration of the implant components, end-to-end *in vitro* system characterizations, and results for the electrical stimulation of a sciatic nerve, demonstrate the feasibility and efficacy of the proposed stimulator for peripheral nerves.**

***Index Terms*—Electroceuticals, implantable medical devices (IMD), peripheral nerve, electrical stimulation, optogenetics, high compliance voltage, electrode characterization, sciatic nerve, EMG.**

I. Introduction

FUTURE medicine will be revolutionized by implantable 'electroceuticals' that target neural pathways for therapeutic intervention, as opposed to prevalent pharmacological approaches [1]. Stimulation of the peripheral nervous system (PNS) has shown great promise for the treatment of a range of conditions including: neurological, autoinflammatory, autoimmune, cardiovascular diseases, and diabetes [1], [2]. For instance, vagus nerve stimulation is effective for the treatment of epilepsy, rheumatoid arthritis, inflammatory bowel disease, and diabetes [1]-[3], sacral and pudendal nerve stimulation can facilitate bladder control [4], [5], and ethmoid nerve stimulation can be used to treat dry eye disease [6].

Aggressive miniaturization of neurostimulators to millimeter (mm) dimensions is essential for avoiding invasive surgery, and the associated post-surgery trauma and infection [7], [8]. This necessitates wireless powering to eliminate bulky batteries and wired interfaces. The stimulator must also be capable of targeting nerves located deep inside the body (>5 cm) for human applications. Further, stimulation is an energy-intensive function, typically requiring a large average load power (up to a few mWs) [9], much greater than temperature or pressure sensing [10], [11], neural recording [12], or data communication [13] (especially using backscatter modulation [14]). Achieving high output power capability simultaneously with a large "depth-to-size ratio" (ratio of tissue depth to implant volume), while complying with long-term safety limits, is a major engineering challenge for stimulators.

Wirelessly powered stimulators have been rapidly evolving over the past decade [15]–[26]. Pioneering work by researchers has led to several optimized designs of neurostimulators using RF near-field, mid-field, and far-field power transfer [16]–[19]. Ultrasonic power transfer is an emerging alternative approach for implants [15], [22], [23], [27]–[29], and has several key advantages, including: (i) energy focusing at large depths (>10 cm) to a mm spot size which enables high power transfer efficiency compared to RF far-field powering [28], [30]–[32], (ii) superior transduction efficiency due to ~mm wavelength [27], [33], and (iii) low tissue attenuation (~0.5-1 dB/cm/MHz) [34].

Ultrasonically powered implants have been demonstrated before [15], [22], [23], [27], including designs using discrete components for electrical [22] or optogenetic stimulation [23]. However, existing literature lacks a miniaturized high voltage (HV) stimulation implant, enabled by a custom-designed IC, for fully programmable and precise control of stimulation parameters. HV compliance (typically >10 V) is desirable for

This material is based upon work supported in part by the DARPA Young Faculty Award (YFA), National Science Foundation (NSF) CAREER Award under Grant ECCS-1454107, NSF Graduate Research Fellowships Program under Grant DGE-114747, and Stanford internal seed funds including SystemX Alliance.

J. Charthad, T. C. Chang, A. Sawaby, M. J. Weber, and A. Arbabian are with the Electrical Engineering Department, Stanford University, Stanford, CA 94305 USA (email: jayantc@stanford.edu, tcchang3@stanford.edu, asawaby@stanford.edu, mjweber3@stanford.edu, arbabian@stanford.edu).

Z. Liu was with Stanford University, Stanford, CA 94305, USA. He is now with the Department of Electrical Engineering and Computer Science, University of California Berkeley, Berkeley, CA 94720, CA, USA (email: zhaokai_liu@berkeley.edu).

S. Baker and S. A. Felt are with the Department of Comparative Medicine, Stanford University, Stanford, CA 94305 USA (email: sambaker@stanford.edu, felt@stanford.edu).

F. Gore is with the Department of Bioengineering, Stanford University, Stanford, CA 94305 USA (email: fgore@stanford.edu).

Digital Object Identifier 10.1109/TBCAS.2018.2799623

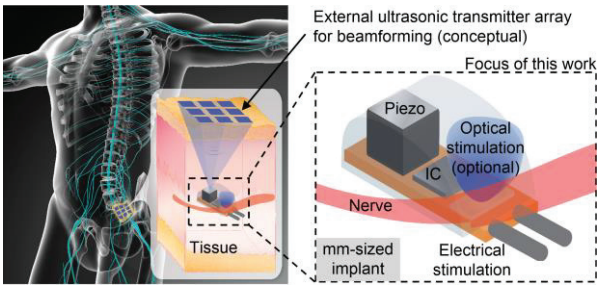

Fig. 1. Conceptual diagram showing operation of our proposed electrical stimulation implant (focus of this work).

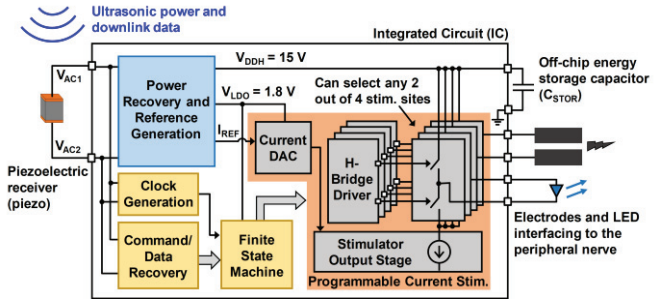

Fig. 2. Implant system architecture and block diagram of the IC.

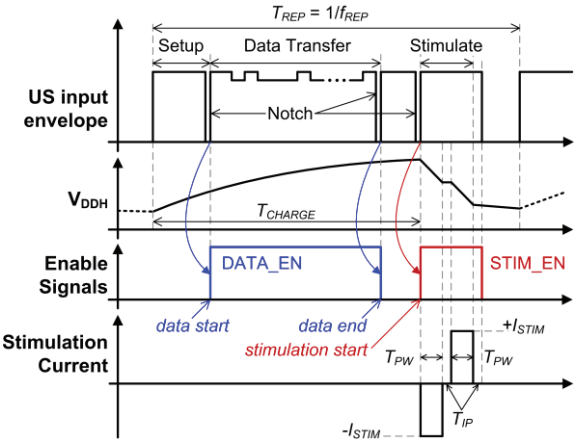

Fig. 3. Timing protocol for power transfer, downlink data communication, and stimulation.

overcoming the effect of tissue encapsulation in chronic applications [35]. Further, while most conventional neurostimulators use exclusively electrical [15], [17], [21], [22] or optical [16], [23] stimulation modalities, a mm-sized *combined electrical/optical stimulator* can have significant value both clinically and as a research tool for mapping neural circuits. Such a "multi-modality" neurostimulation platform can enable cell-type-specific stimulation by leveraging the high spatial resolution of optogenetics [36], as well as recruitment of a large number of nerve fibers (e.g. to generate a large muscle force [37]) through electrical stimulation. [19] demonstrates a highly efficient electrical/optical stimulator with thorough *in vitro* and *in vivo* characterization results. However, their demonstrated power transfer range is 1 cm (sufficient for their application of deep brain stimulation in rats), and the implant is not miniaturized to mm dimensions.

In order to address the above challenges, we demonstrate a fully integrated electrical stimulation implant, along with an optional LED, as shown conceptually in Fig. 1. An external transmitter (TX) beams ultrasonic power and downlink (DL) data to the implant, allowing fully programmable stimulation of a peripheral nerve. The principal focus of this paper is on the design of a proof-of-concept mm-sized stimulation implant, and demonstration of its functionality using a commercial external ultrasound TX at great depths. Implementation of a custom conformal TX array conceptually shown in Fig. 1, and optimization of the end-to-end power transfer efficiency (PTE) of the ultrasonic link, are parts of future work. This is possible because far-field power transfer allows independent optimization of the external TX (as demonstrated in [28], [30], [31]) and the receiver (implant) [27], [33], as opposed to near-field powering systems. The implant is miniaturized to 2×3×6.5 mm^3, and operates well below the FDA diagnostic ultrasound intensity limit (7.2 mW/mm^2) at a depth of 10.5 cm in a tissue phantom. Despite the use of a commercial TX which was not optimized for this application, the achieved depth of operation is unprecedented for programmable neural stimulation implants. This implant achieves a depth/volume FOM of 2.7 mm^{-2} which is >10× higher than state-of-the-art programmable neurostimulators.

This paper presents co-design of the piezoelectric receiver (piezo) and IC for complete operation during the charging transient of the storage capacitor (section III), a downlink command and data transfer protocol (section IV), design and characterizations of the stimulation electrodes and a commercial LED (section VI), and *in vitro* characterizations along with preliminary *in vivo* results demonstrating functionality (section VII). Two types of *in vitro* measurements are presented – detailed system characterization (section VII-A) with access to internal nodes of the implant, and "blind" tests of the fully integrated implant (section VII-B) with access only to the electrode/LED terminals for verifying stimulation patterns. Finally, results for the electrical stimulation of a sciatic nerve are presented (section VII-C), and the overall performance of the implant is compared with state-of-the-art (section VII-D). Robust biocompatible packaging, *in vivo* tests of the fully packaged implant, and *in vivo* optogenetic stimulation experiments, are a part of future work.

II. Implant System Overview

The implant (Fig. 2) comprises a piezo, an IC, an off-chip storage capacitor (C_{STOR}), two stimulation electrodes, and an LED, all integrated into a mm-sized package. Major blocks in the IC include: power recovery, command/data recovery, and a programmable current stimulator.

The power recovery circuit extracts and conditions the power received by the piezo, and charges C_{STOR} to V_{DDH}. Additionally, this block generates a regulated DC supply rail (V_{LDO} = 1.8 V) for reliably powering other circuits, and a reference current (I_{REF} = 2 µA) for stimulation. While V_{DDH} is targeted to be >12 V for worst-case electrical stimulation parameters (HV compliance required due to encapsulation tissue), our system is flexible such that C_{STOR} can also be charged to lower voltages sufficient for driving an LED (forward voltage ≈ 3 V) for

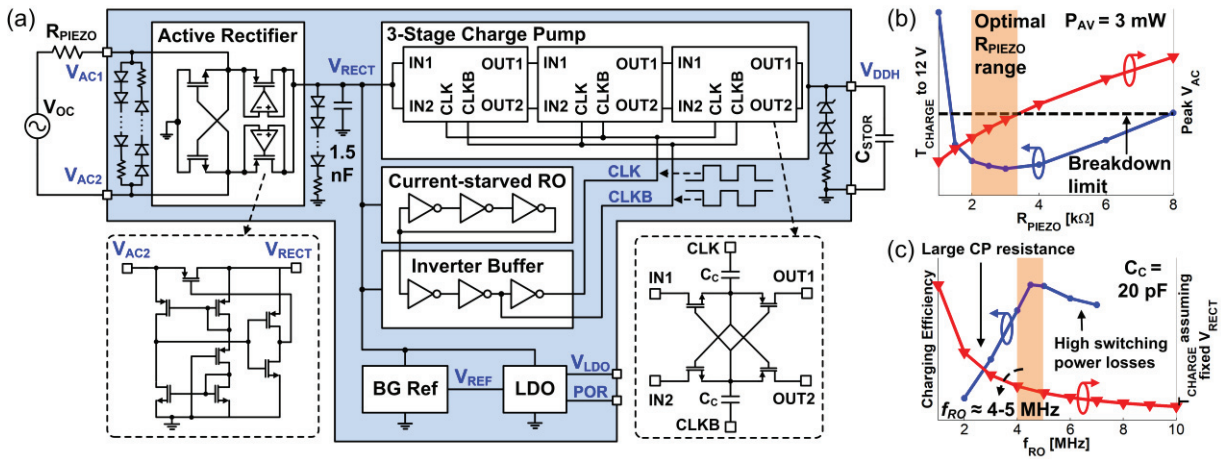

Fig. 4. (a) Schematic diagram of the power recovery circuit, (b) simulation-based analysis of the optimal range of R_{PIEZO} for P_{AV} = 3 mW, (c) simulation-based analysis of the design choice of f_{RO} for C_C = 20 pF.

efficient optical stimulation, or if the electrode/tissue interface impedance is low for a particular application.

The data/command recovery and clock generation circuits extract stimulation parameters from the incoming US signal. A finite state machine (FSM) interprets these parameters and controls the stimulator to produce a stimulation waveform with the desired current amplitude (I_{STIM}), and pulse-width (T_{PW}), between the desired pair of stimulation sites. The repetition rate of stimulation (f_{REP}) can be precisely controlled externally by the transmitter and is, therefore, not encoded in the DL data bits, thereby also simplifying data recovery design. This system allows full configurability of the stimulation pattern/modality from cycle-to-cycle which is useful for rapidly adapting stimulation during closed-loop operation, or having variable time intervals between consecutive stimulation pulses, if desired.

Fig. 3 shows our system timing diagram for the most energy-intensive stimulation pattern (worst-case). A notch-based communication protocol, as further explained in section IV, is used for sending DL commands to enable/disable the command/data recovery circuit, and to initiate the stimulation event. DL data bits are transmitted simultaneously during the charging of C_{STOR} in order to minimize the total setup time before stimulation. In this architecture, the stimulation current is directly supplied by C_{STOR}. Ultrasound is kept ON during stimulation to provide a timing reference for T_{PW}, and to supply power to other circuit blocks, thereby avoiding the need for additional off-chip energy storage capacitors (e.g. on V_{LDO} rail).

For minimizing design complexity, the stimulator core is primarily designed based on the stringent constraints imposed by electrical stimulation, and re-used for optical stimulation. The stimulator generates a biphasic current-controlled waveform, with balanced cathodic and anodic phases, and an inter-phasic delay (T_{IP}) for higher stimulation efficacy [35], [38], as shown in Fig. 3. I_{STIM} is programmable on a wide scale of 22 to 5,000 µA, T_{PW} is programmable from ~14 to 470 µs, while f_{REP} can be controlled externally between 0 to 60 Hz. Further, for electrical stimulation, the threshold current is known to decrease with increasing pulse-width [39], [40]. Based on this, and to limit the energy requirements of the implant, we design the electrical stimulator for providing a maximum stimulation charge, $Q_{STIM,MAX}$, of 300 nC (total value for two phases), which is >5× the threshold charge required to elicit *in vivo* response in the sciatic nerve of a frog, as demonstrated in section VII-C. Note that while applications such as deep brain stimulation (DBS) may require total stimulation charge > 300 nC, and repetition rates > 100 Hz, our stimulator is specifically designed for peripheral nerves with stimulation parameters that are known to be effective for PNS applications [3], [38], [41]. Further, optogenetic stimulation has been demonstrated by researchers with optical intensities > 1 mW/mm^2 [16], [42]. While our stimulator is designed to support optical intensities up to 23 mW/mm^2, and pulse-widths up to ~470 µs, the range of pulse-widths can be extended to ~ms in future designs for more flexibility in choosing optogenetic stimulation parameters for *in vivo* applications.

The stimulator (Fig. 2) comprises an 8-bit current DAC, an output stage, and an H-bridge. H-bridge configuration allows the use of a single current source for both stimulation phases, which is advantageous for achieving charge balance [43]. The H-bridge interfaces with four stimulation sites, any two of which can be selected by the DL data bits to perform stimulation across them.

As a part of future work, adiabatic stimulation architectures, as demonstrated in [44]–[46], can be implemented for optimizing stimulation efficiency. Implementation of a greater number of stimulation channels, as demonstrated by highly integrated state-of-the-art stimulators for the brain [47], retina [48], [49], spinal cord [17] and cochlear [50] applications, can be investigated in the future. Other functions such as a data uplink and neural recording, while not necessary for this implant, can also be incorporated, in addition to techniques for simultaneous neural stimulation and recording, as thoroughly discussed in [51], [52] to enable a complete implant system for closed-loop neuromodulation [52], [53].

III. Power Recovery Design

In order to store sufficient charge for worst-case electrical

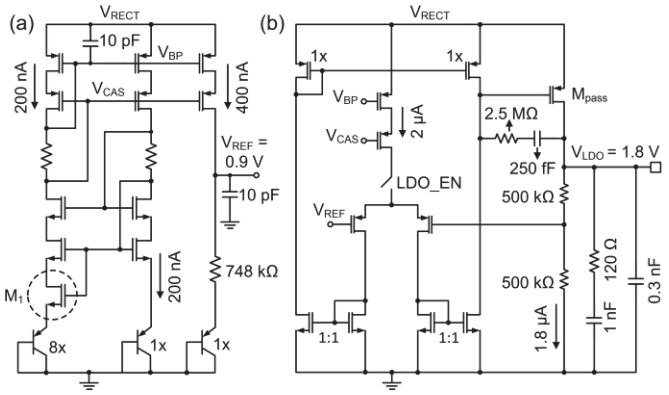

Fig. 5. Schematic diagrams of (a) the bandgap reference circuit, and (b) the LDO circuit.

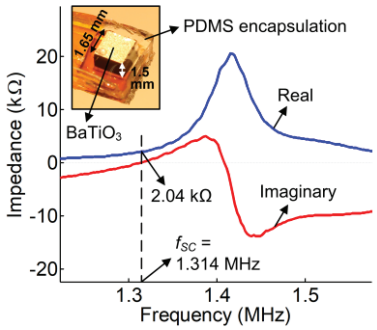

Fig. 6. Measured impedance profile of the 1.65×1.65×1.5 mm^3 $BaTiO_3$ piezoelectric device encapsulated with PDMS.

stimulation parameters ($Q_{STIM,MAX}$ = 300 nC), we choose C_{STOR} to be ~40 nF, resulting in stored charge, $Q_{STOR} \approx$ 480 nC, for V_{DDH} = 12 V. Based on the timing diagram in Fig. 3, it can be noted that, for a maximum T_{PW} of 470 µs, and T_{IP} of ~80 µs, T_{CHARGE} should be limited to a maximum of ~15 ms for achieving a maximum f_{REP} of 60 Hz. Thus, the power recovery circuit is designed with the objective of achieving T_{CHARGE} < 15 ms.

The overall architecture of the power recovery circuit is adapted from [27], and is presented in Fig. 4 (a). It primarily comprises an active rectifier and a charge pump (CP), where the CP clock is generated by a current-starved ring oscillator (RO), followed by an inverter buffer [27]. As shown in Fig. 4 (a), the circuit also includes AC voltage limiting clamps between nodes V_{AC1} and V_{AC2} (limiting peak voltage to ~4.5 V), and DC clamps on V_{RECT} (voltage limit of ~4.5 V) and V_{DDH} (voltage limit of ~18 V) rails, to prevent circuit breakdown if high ultrasonic power is delivered to the implant during *in vivo* operation. It is important to note that, while [27], [29] and [33] are based on a steady-state analysis of power flow, this design is more complicated due to operation during the charging transient of C_{STOR}. Therefore, we perform a simulation-based analysis as discussed below to choose values for the major design variables.

We first consider the design constraints imposed by the ultrasonic link and the piezo. The average acoustic intensity ($I_{ac,avg}$) should be kept below the FDA regulated spatial peak temporal average intensity (I_{SPTA}) of 7.2 mW/mm^2. Further, as discussed in [27], [33], mm-sized piezos are intentionally designed to achieve resonant impedance (R_{PIEZO}) in the ~kΩ range precluding the use of a bulky input matching network, and leading to high voltages at the input of the IC for ~mW level available powers (P_{AV}). This sets a limit on peak P_{AV}, and consequently, the peak acoustic intensity at the piezo. Thus, the major design variables related to the ultrasonic link and the piezo are P_{AV} and R_{PIEZO}. Due to non-linearity of the power recovery circuit, especially during the charging of C_{STOR}, we perform simulations for the circuit in Fig. 4 (a) to analyze the optimal range of R_{PIEZO} for a fixed P_{AV} of 3 mW. This value for P_{AV} is chosen in order to reliably maintain peak IC input voltage < 4.5 V (below the activation threshold of the voltage limiting clamps). As shown in Fig. 4 (b), R_{PIEZO} in the range of 2-3.5 kΩ was determined to be optimal for this design.

Next, we consider the design constraints related to the power recovery circuit blocks. The major design variables for this circuit are the RO frequency (f_{RO}), the CP coupling capacitance (C_C), and the number of CP stages (N), which have to be chosen for meeting the V_{DDH} and T_{CHARGE} requirements in this design. N is chosen to be 3 for achieving V_{DDH} > 12 V while operating at an input voltage amplitude of ~3-4 V. This input voltage amplitude is a result of our design choice of P_{AV} (3 mW) and R_{PIEZO} (2-3.5 kΩ). The value of C_C is chosen as 20 pF based on area considerations because the area of a CP is typically dominated by the total pumping capacitance ($2\times C_C \times N$) [54]. Further, assuming a constant value of V_{RECT} at the input of the CP for simplicity, and using a dynamic model of capacitively loaded CPs as discussed in [54], it is intuitive that a large product of f_{RO} and C_C is desirable for minimizing the charging time of C_{STOR}. However, for the complete power recovery chain with a fixed P_{AV}, a high f_{RO} would lead to a high switching power dissipation in the RO and the inverter buffer, thereby, providing lower input power to the CP for the charging of C_{STOR}. Based on this trade-off, and C_C of 20 pF, we perform simulations of the charging efficiency, and choose f_{RO} in the range 4-5 MHz, as shown in Fig. 4 (c). The choice of f_{RO} was limited to 5 MHz in order to minimize sensitivity of the RO frequency to layout parasitics.

A full-wave active rectifier with self-startup capability, as discussed in [27], [55], is implemented at the input of the IC for achieving a high AC-DC voltage conversion ratio (VCR). A 1.5 nF on-chip output capacitor minimizes voltage ripple, without significantly affecting rectifier startup time. A latched topology is used for the charge pump for achieving a high VCR. A bandgap reference (BGR), presented in Fig. 5 (a), generates a reference voltage (V_{REF} = 0.9 V) and current (I_{REF} = 200 nA). The BGR is implemented using an NMOS transistor (M_1) in the linear region, as opposed to a resistor, to reduce chip area and minimize process variation. Design across a wide temperature range, and the associated curvature-correction techniques, are not extremely important for this application due to small variations of body temperature (< ±3 °C). The BGR has a simulated power supply rejection ratio (PSRR) of -53.6 dB at the power carrier frequency of ~1.3 MHz (discussed below).

The LDO, as shown in Fig. 5 (b), uses a PMOS pass transistor, and a current-mirror OTA as error amplifier. Miller compensation, a series RC branch (120 Ω, 1 nF), and an

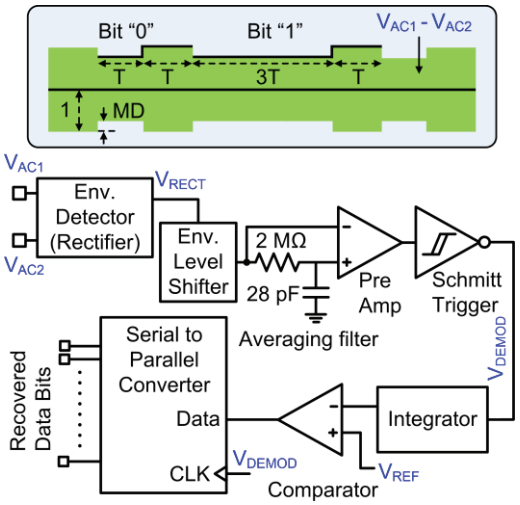

Fig. 7. Schematic diagram of the data recovery circuit.

additional 0.3 nF on-chip load capacitor guarantee stability and robust transient performance across a wide range of load currents (0 to 1 mA). The LDO consumes a quiescent current of 5.8 µA, and is designed to achieve a loop bandwidth of ~100 kHz at no load and ~2 MHz at full load (1 mA), achieving worst-case load/line transient variation of <150 mV in simulations. Simulated PSRR of the LDO at the powering frequency of ~1.3 MHz is -56.7 dB at no load and -23 dB at full load. PSRR at full load is sufficient because the 1.5 nF on-chip capacitor at the output of the rectifier limits the peak-to-peak supply voltage ripple to ~100 mV.

Finally, the design of the piezo and choice of the power carrier frequency are based on principles outlined in [27] and [33]. Barium titanate ($BaTiO_3$) is chosen as the piezo material for biocompatibility [56]. We choose a thickness of 1.5 mm to achieve short-circuit resonance frequency (f_{SC}) in the low ~MHz range (advantageous due to low tissue losses), and limit the overall package height to ≤ 2 mm. Lateral dimensions of the piezo are chosen as 1.65×1.65 mm^2 to achieve a resistance of 2 kΩ at f_{SC}, which lies in the optimal R_{PIEZO} range for charging C_{STOR} within the target time. An air-backed structure is used for achieving a high acoustic-to-electrical power conversion efficiency or aperture efficiency (η_{ap}) for the piezo [33]. Fig. 6 shows a picture of the piezo package, and its measured impedance profile. The power carrier frequency is precisely chosen as 1.314 MHz because it is the measured f_{SC} of the piezo as shown in Fig. 6. The measured η_{ap} at f_{SC} is between 30-40% for different samples (similar to [33]).

IV. Downlink (DL) Command/Data Recovery Design

The choice of our DL protocol and architecture is motivated by the need to accomplish command and data transfer with minimal impact on power recovery during the charging transient of C_{STOR}, where the voltage amplitude on the piezo terminals (V_{AC}) is not constant. Our protocol comprises three independent commands (see Fig. 3): *data start*, *data end,* and *stimulation start*, each transmitted in the form of a notch in the ultrasound power-up signal (30-50 µs OFF time). The data recovery circuit is only enabled between the *data start* and *data end* commands to minimize overall energy consumption. The *stimulation start* command initiates the stimulation pulse. This protocol allows independent and programmable external control over the timing of data transfer and stimulation. The core circuit for notch detection generating 'DATA_EN' and 'STIM_EN' signals (Fig. 3), was adapted from [27].

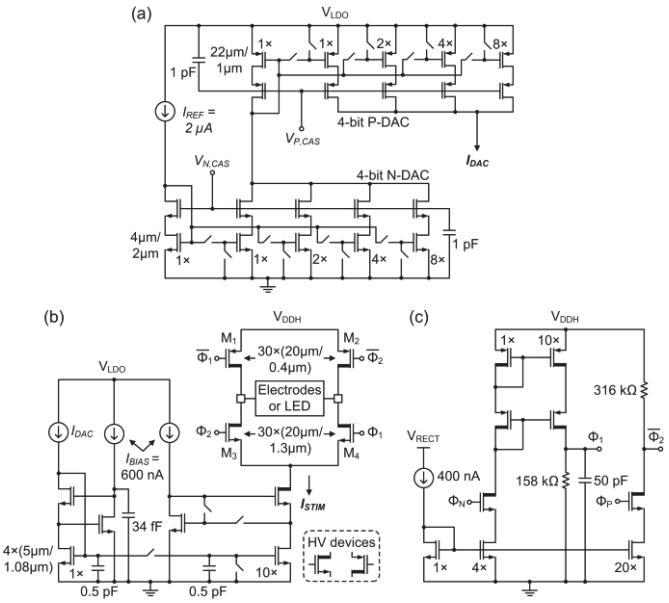

Fig. 8. Schematic diagrams of (a) current DAC, (b) stimulator output stage, and (c) H-bridge driver.

After the *data start* command, pulse-width modulated amplitude-shift keying (PWM-ASK) [57], [58] is used for data transfer to program the stimulation modality or channel (4 bits), I_{STIM} (8 bits) and T_{PW} (5 bits) – a total of 17 programming bits for each stimulation pulse. As shown in Fig. 7, bits "0" and "1" are defined by amplitude modulation of the input ultrasound power signal, and are distinguished from each other by the duration for which the ultrasound envelope is low (T for bit "0", versus $3T$ for bit "1", where nominally, T=30 µs). This scheme enables asynchronous operation of the implant where the clock is extracted from the bit envelopes without using a dedicated timing reference for decoding [59]. The active rectifier is reused for envelope detection, and is followed by a level shifter, an averaging filter, and an integrator-based demodulator, as shown in Fig. 7. The averaging filter generates a moving threshold for comparison with the envelope, which is essential due to the variation in V_{AC} during the charging of C_{STOR}. The simulated total energy consumption of the data recovery circuit block for T = 30 µs is 1.25 nJ/bit. This design achieves amplitude modulation depth (MD) as low as 3% at the piezo/IC terminals (implying minimal impact on power recovery), with a bit error rate (BER) of $<10^{-5}$ and a data rate of 11 kbps, as verified by measurements discussed in section VII.

V. Stimulator and FSM Design

Based on the recovered data bits, an 8-bit current DAC sets the value of I_{STIM}. A segmented architecture was chosen for the DAC which comprises two 4-bit binary DACs (N-DAC and P-DAC), as shown in Fig. 8 (a) [43]. This architecture avoids

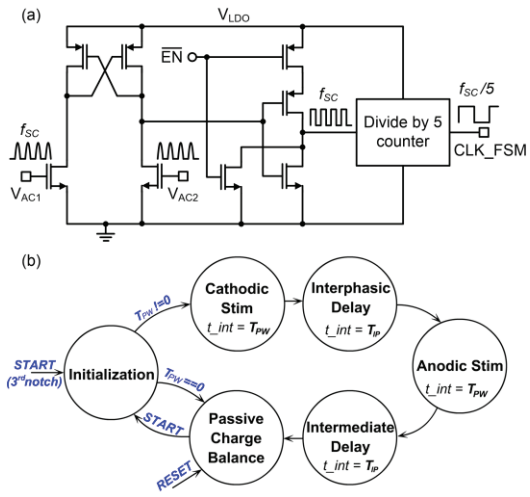

Fig. 9. (a) Schematic diagram of the clock recovery circuit, (b) operation of the finite state machine (FSM).

extremely large current mirroring ratios of an 8-bit binary-weighted DAC, thus, allowing better layout matching for the current mirrors. The output current of the DAC (I_{DAC}) is given by:

$$I_{DAC} = I_{REF} \times \left\{\sum_{n=0}^{3}(2^n d_n)\right\} \times \left\{\sum_{p=0}^{3}(2^p \overline{d_p})\right\}, \qquad (1)$$

where, d_n and d_p represent the binary bits corresponding to the N-DAC and the P-DAC, respectively, and $\overline{d_p}$ is the one's complement of d_p. It can be noted that the value of the least significant bit (LSB), or resolution of the DAC, is commensurate with its output current range. For instance, for small I_{DAC} in the range 2-30 µA, the LSB is 2 µA, whereas, for large I_{DAC} in the range 30-450 µA, the LSB is 30 µA. This design achieves maximum voltage headroom of ~200 mV for the N-DAC, and between 300-400 mV for the P-DAC. Mismatch simulations show that the ±3σ variation in I_{DAC} is ±8.5% at 2 µA, and < ±5% at 450 µA.

The stimulator output stage shown in Fig. 8 (b) comprises a single 1:10 wide-swing NMOS cascode current mirror which generates $I_{STIM} = 10I_{DAC}$. A regulated cascode topology based on Sackinger implementation is used for achieving a high output impedance (> 25 MΩ for I_{STIM} = 4.5 mA in simulation). A 24 V LDMOS transistor serves as a cascode device on the output side for HV operation. Worst-case simulated voltage headroom is < 1.0 V for I_{STIM} of ~5 mA across all process corners. During stimulation, the voltage across the stimulator output stage is always ensured to be > 1 V, even with practical electrode impedances and maximum stimulation current. Thus, there is minimal change in the stimulation current value during the cathodic and anodic stimulation phases, despite large variations in V_{DDH} or voltage on the electrode terminals. Further, mismatch simulations show that ±3σ variation in I_{STIM} is ±9.3% at 20 µA (< 1 LSB = 20 µA), and ±5% at 4.5 mA (< 1 LSB = 300 µA).

Switches in the H-bridge (M_1-M_4) are implemented using HV devices with a 20 V $|V_{DS}|$ breakdown limit. Due to unavailability of devices with a high (> 5 V) gate-oxide breakdown limit, the H-bridge drivers, as shown in Fig. 8 (c), incorporate level shifter circuits to reliably limit $|V_{GS}|$ of M_1-M_4 to < 5 V. The large drain-bulk diodes of M_1-M_4 (due to their large size for minimizing ON resistance) provide ESD protection for the electrode/LED terminals [48]. Passive charge balance is achieved by shorting the electrode terminals at the end of each stimulation cycle, in addition to using a single current source for both phases, which was found to be sufficient for this application as further discussed in section VII-A. Several other techniques for charge balancing, applicable to different stimulator architectures, have been demonstrated by other researchers [60], [61], and can be considered for future implementations of this implant.

A clock recovery circuit senses the AC voltage on the piezo terminals (Fig. 9 (a)) in order to extract timing information from the incoming US signal for T_{PW} control. It comprises a latch with an inverter output stage, followed by a divide-by-5 counter to generate a signal with frequency f_{SC}/5 which serves as the clock for the FSM (CLK_FSM signal). The clock recovery circuit is enabled only after the *data end* command to minimize its energy consumption. Since the US input amplitude (> 2.5 V) is always greater than the threshold voltage (~0.85 V) of the input transistors of the latch, the CLK_FSM signal is not affected by variations in the US input amplitude.

The states and operation of the FSM are described in Fig. 9 (b). For robust operation, the FSM includes an initialization period comprising a delay of two cycles (~7.6 µs) of the CLK_FSM signal after the third notch. This ensures that all control signals, including CLK_FSM, required for defining the stimulation pulse are in steady-state before the actual beginning of the pulse. The interphasic delay, T_{IP}, is set equal to T_{PW} for T_{PW} = ~14 µs, and half of T_{PW} for T_{PW} < ~150 µs, beyond which it is fixed at ~75 µs for larger pulse-widths [35].

VI. Electrode and LED Characterization

The choice of stimulation electrodes for this design was primarily guided by requirements of safety, miniaturization, achieving low electrode impedance, and a high charge storage capacity [62] for supporting the worst-case stimulation parameters. We use two Platinum (Pt) wires of 2 mm length and 0.5 mm diameter as stimulation electrodes. Platinum is chosen because it allows charge injection through double-layer charging and reversible faradaic reaction mechanisms, which are considered safe for both the tissue and the electrodes [62]. Further, the electrode dimensions are chosen to achieve sufficient geometrical surface area (~3.3 mm^2 or 0.033 cm^2 per electrode) to limit maximum charge density (~5 µC/cm^2) well below electrode and tissue damage thresholds [62].

As shown in Fig. 10 (a), the electrodes have a measured impedance of < 1 kΩ at 1 kHz in 1× phosphate buffered saline (PBS) solution (pH = 7.4), which models dielectric properties of tissue. This low measured impedance, coupled with a high stimulator compliance voltage (>12 V) will enable chronic applications. Fig. 10 (b) shows measured cyclic voltammograms of our electrodes in 1× PBS demonstrating a charge storage capacity (Q_{CS}) of ~120 µC within the water

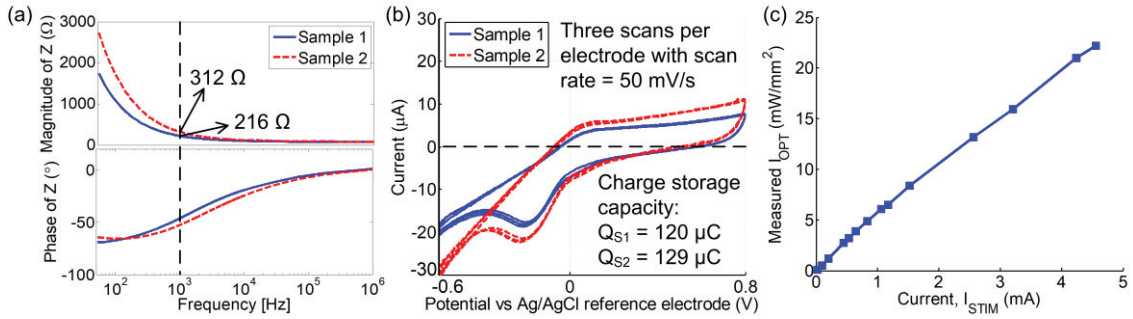

Fig. 10. (a) Measured impedance, and (b) measured cyclic voltammograms (CV) of the 2 mm Pt electrodes in 1× PBS solution; (c) optical intensity (I_{OPT}) of the blue LED measured using a photodiode placed ~500 µm away from the LED.

window for Pt (–0.6 V to 0.8 V versus Ag|AgCl). Measured Q_{CS} is several orders of magnitude greater than maximum stimulation charge per phase of 150 nC, implying that the electrodes can be further miniaturized in future designs based on their performance in chronic *in vivo* studies.

Further, we performed measurements of a commercial blue LED (Rohm SMLP13BC8T), with a dominant wavelength of ~470 nm, and an active area of 0.04 mm^2, to characterize its optical intensity as a function of I_{STIM}. This wavelength is typically used to activate channelrhodopsin (light-sensitive protein) in optogenetic applications [24], [36]. Optical intensity was measured using a photodiode (ThorLabs FDS1010) placed at a distance of ~500 µm from the LED. The LED was also encapsulated with a thin layer of PDMS to model the final implant package. Fig. 10 (c) shows that optical intensities up to ~23 mW/mm^2 can be achieved (exceeding requirements of optogenetic stimulation [63]) for I_{STIM} up to ~5 mA. Voltage drop across the LED is ≤2.9 V, implying that it can be easily driven by our stimulator with a much larger supply voltage capability (>12 V).

VII. Implant Measurement Results

A. In Vitro Implant Characterization

The IC was fabricated in TSMC 180 nm HV BCD process and measures 1.48 mm × 2.42 mm (3.58 mm^2), as shown in Fig. 11. *In vitro* implant characterization was performed using the setup shown in Fig. 12. This setup allows accurate characterization of the system with ultrasonic powering and data transfer at a large depth of 10.5 cm, along with extensive probing of the IC for detailed operation analysis. The piezo, fully encapsulated with PDMS (described in section III), is mounted in a tank filled with castor oil, and is wirelessly powered with a focused single-element external ultrasound transmitter (Olympus A392S) with a focal distance of ~10.5 cm. Castor oil is used to model the acoustic impedance and loss of soft tissue (Z = 1.43 MRayls [64], loss = ~0.9-1.2 dB/cm at f_{SC} ≈ 1.3 MHz [65], [66]), while minimizing electrical loading on the piezo. Based on characterization of the transmitter's beam profile with a needle hydrophone, peak acoustic intensity (I_{ac}) at the piezo is estimated to be 2.9 mW/mm^2, resulting in measured P_{AV} of 3 mW ($P_{AV} = \eta_{ap} \times I_{ac} \times A$) for a piezo sample with measured η_{ap} of 38% and area (A) of 2.72 mm^2. For a maximum f_{REP} of 60 Hz, the time-averaged acoustic intensity is ≤ 2.4 mW/mm^2 (worst-case) which is 3× below the FDA I_{SPTA}

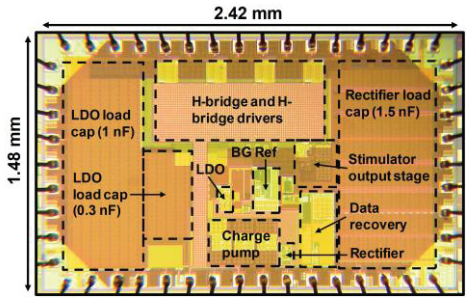

Fig. 11. Die photo of the IC.

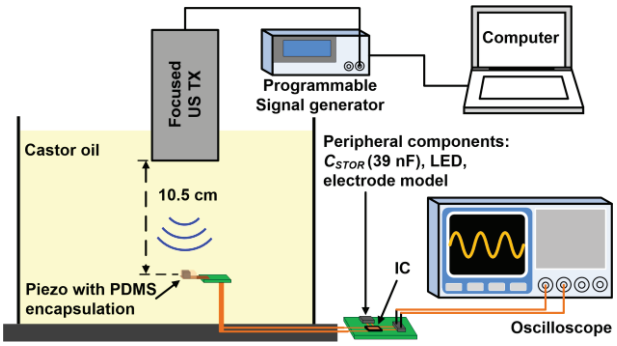

Fig. 12. *In vitro* implant characterization setup with ultrasonic powering and data transfer at 10.5 cm depth in castor oil, as well as access to internal implant nodes for detailed operation analysis.

limit. The measured receiver η_{ap} is >30 % for all samples. Combined with a custom external ultrasound array [28], [30], [31], this system can achieve a high link PTE approaching ~1-2%, which is challenging for depths >10 cm. For instance, [28] achieves a measured PTE of 1.6% at a depth of 10.5 cm (9.5 cm tissue phantom and 1 cm water), although not for neural stimulation applications. Our current setup is limited to a measured PTE of 0.04% (-34 dB) due to use of a single-element off-resonant commercial transducer. Based on measurements and simulations using COMSOL Multiphysics, the total PTE of -34 dB is estimated to comprise of the following components: (i) -13 dB due to attenuation in 10.5 cm of castor oil, (ii) -8.6 dB due to directivity of the TX, (iii) -8.2 dB (or 15.1%) electrical-to-acoustic conversion efficiency of the TX, and (iv) -4.2 dB (or 38%) aperture efficiency of the piezo. Although the wireless powering depth and PTE are currently limited by our experimental setup, and can be optimized even further through the design of a custom TX array (optimizing components (ii) and (iii) of the efficiency), our work demonstrates the largest

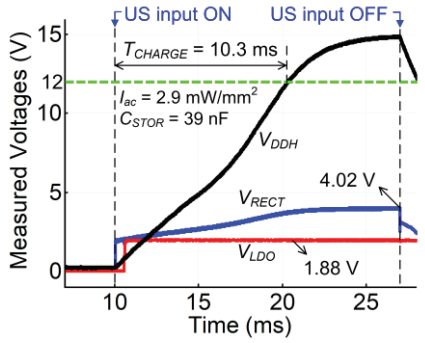

Fig. 13. Measured power recovery waveforms during the charging of C_{STOR}.

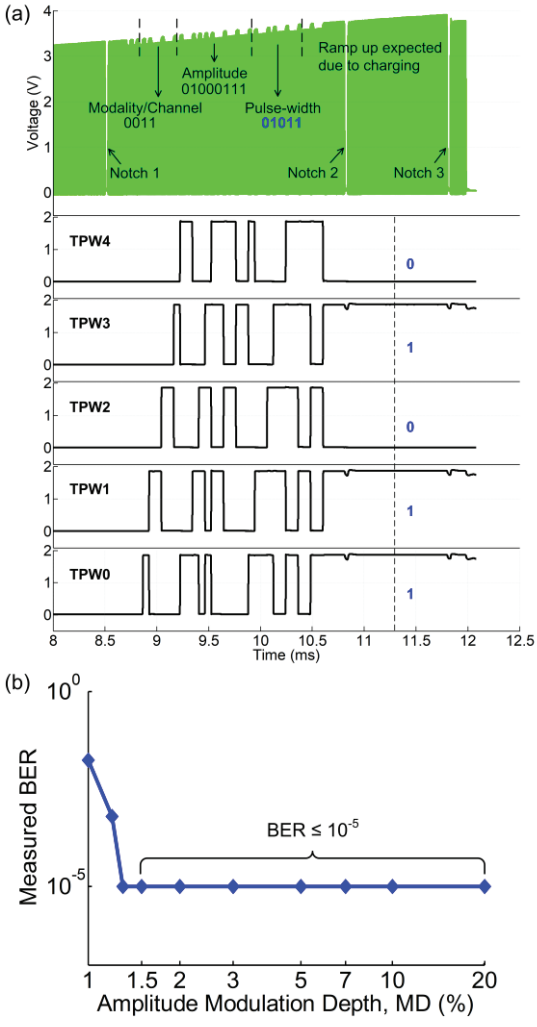

Fig. 14. (a) Example of recovered bit waveforms showing measured pulse-width control bits (TPW4-TPW0), (b) measured bit error rate (BER) as a function of amplitude modulation depth (MD).

depth in a tissue phantom among other IC-based fully programmable stimulation implants of comparable or even larger sizes, while operating 3× below the FDA I_{SPTA} limit.

The equivalent half-power beam diameter of our focused transmitter at 10.5 cm depth is measured to be 3.3 mm (2× the lateral dimension of the piezo). Thus, the link can be affected by misalignment, primarily due to the focused nature of the transmitter. To partially mitigate this effect, a combination of ultrasound imaging [67], [68] and transmit beamforming [28],

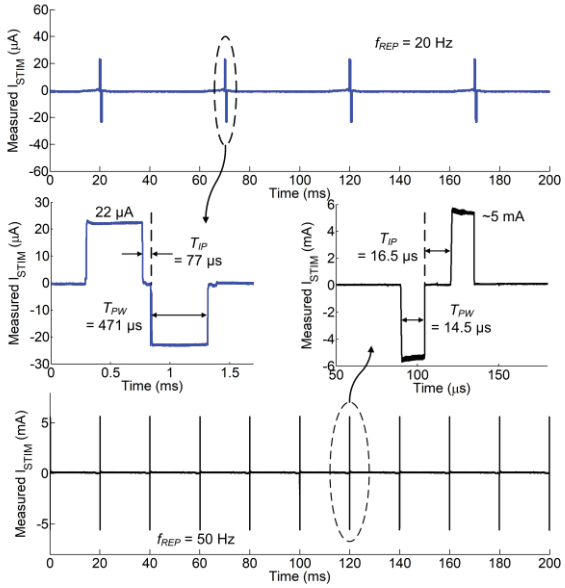

Fig. 15. Measured stimulation current waveforms.

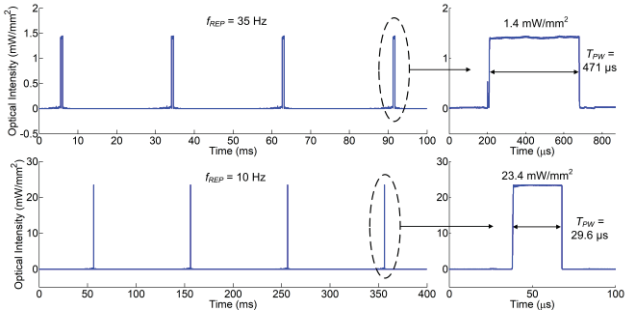

Fig. 16. Optical stimulation patterns based on measured current waveforms through the blue LED (driven by the implant IC using the characterization setup of Fig. 12), and the LED characterization result of Fig. 10 (c).

[69] functions could be implemented on the external device in the future, in order to locate the implant and direct the ultrasound beam towards it. These functions have been individually demonstrated before with mm or sub-mm precision at > 10 cm tissue depths [28], [67]. In addition, future systems must also maximize the acceptance angle of the piezo to achieve robust link operation.

Fig. 13 shows power recovery waveforms during the charging of C_{STOR}. During charging, the output voltage of the rectifier (V_{RECT}) varies from ~2.5-4.02 V, resulting in a measured VCR of 92%. V_{DDH} reaches the target value of 12 V within 10.3 ms (T_{CHARGE}), allowing for a maximum f_{REP} of ~85 Hz which is well beyond the required specification. Note that for applications requiring compliance voltage <12V, maximum f_{REP} can be >85 Hz. Measured maximum V_{DDH} is 15 V exceeding the HV compliance specification. Measured VCR for the charge pump at the end of the charging cycle is 91%. Further, the critical energy efficiencies were estimated from simulations – the input matching efficiency is 82%, the energy efficiency of the active rectifier is 71.4%, and that of the charge pump is 70.5%.

Wireless data recovery measurements showed reliable recovery of the command signals (notches) and the PWM-ASK

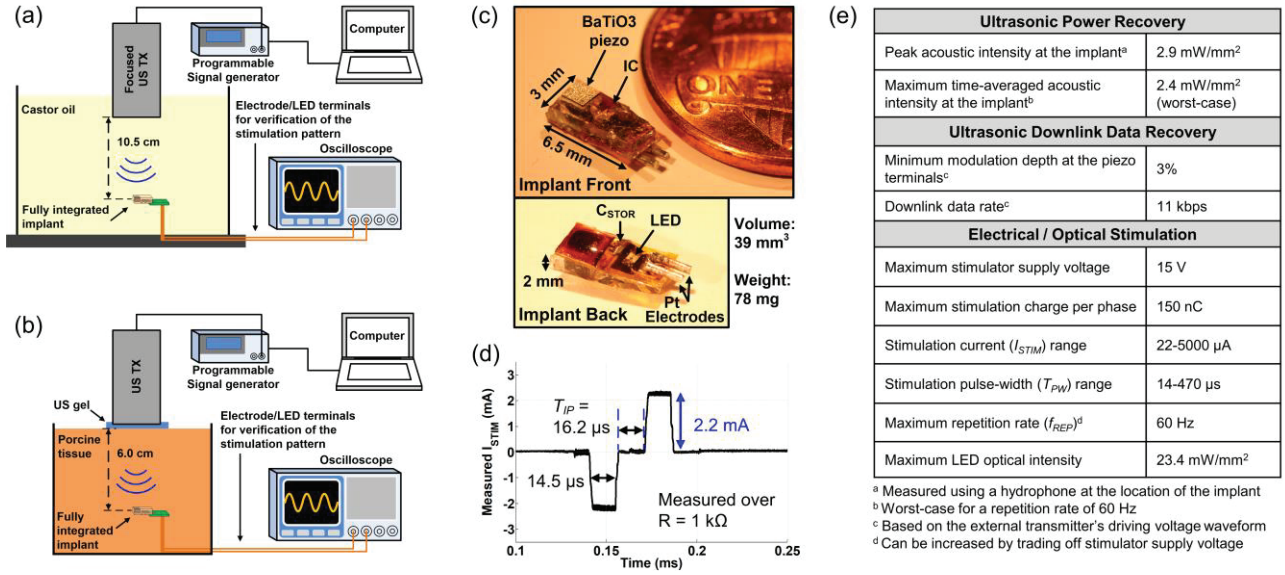

Ultrasonic Power Recovery	
Peak acoustic intensity at the implant[a]	2.9 mW/mm^2
Maximum time-averaged acoustic intensity at the implant[b]	2.4 mW/mm^2 (worst-case)
Ultrasonic Downlink Data Recovery	
Minimum modulation depth at the piezo terminals[c]	3%
Downlink data rate[c]	11 kbps
Electrical / Optical Stimulation	
Maximum stimulator supply voltage	15 V
Maximum stimulation charge per phase	150 nC
Stimulation current (I_{STIM}) range	22-5000 µA
Stimulation pulse-width (T_{PW}) range	14-470 µs
Maximum repetition rate (f_{REP})[d]	60 Hz
Maximum LED optical intensity	23.4 mW/mm^2

[a] Measured using a hydrophone at the location of the implant
[b] Worst-case for a repetition rate of 60 Hz
[c] Based on the external transmitter's driving voltage waveform
[d] Can be increased by trading off stimulator supply voltage

Fig. 17. (a) Measurement setup for the fully integrated implant at a depth of 10.5 cm in castor oil, (b) measurement setup for the fully integrated implant through 6 cm of porcine tissue (limited by our setup for stacking meat slices), (c) picture of the fully integrated stimulation implant, (d) measured current waveform (only zoomed single pulse shown) for the setup in (b), and (e) performance summary of the fully integrated implant for the setup in (a).

modulated DL data bits. As an example, Fig. 14 shows measured waveforms for the pulse-width control bits (TPW4-TPW0) demonstrating that the settled bit values after the second notch (*data end* command) correlate well with the transmitted data signal as seen at the piezo terminals. Our data recovery design achieved a minimum measured MD of 3% (at the piezo/IC terminals) signifying that simultaneous data recovery during power-up can have a minimal impact on the charging of C_{STOR}. Further, the maximum measured MD was 20%, allowing a wide programmable range for the selection of MD based on the trade-off between robustness of data transfer, and charging of C_{STOR}. The measured DL data rate is 11 kbps (since the average bit duration is 90 µs based on Fig. 7 where T = 30 µs) which is sufficient for this application since the transmission of all data bits can be completed well within T_{CHARGE}. To demonstrate the robustness of our data DL, the measured BER as a function of different amplitude modulation depths of the data signal is shown in Fig. 15. For these measurements, the setup in Fig. 12 was used, 100,000 sequences of the 17 programming bits were transmitted across the 10.5 cm wireless link, and zero bit errors were achieved for MD ≥ 1.5%. Thus, the measured BER at a confidence level of ~100% is 10^{-5} for MD down to 1.5% (half of our minimum operating MD of 3% at which all other results are presented). For MD below 1.5%, it is intuitive that BER increases because the difference between the amplitude levels approaches the noise level of the demodulator.

DNL and INL of the N-DAC and P-DAC were measured to be ≤ 0.1 LSB. Fig. 15 shows stimulation current waveforms measured on a series electrode impedance model (1 kΩ, 100 nF). Note that this impedance is greater than the measured impedance of our electrodes in PBS (Fig. 10 (a)) and, thus, presents a worst-case condition for this characterization. Our measurements show reliable generation of stimulation currents in compliance with the programmed stimulation parameters (I_{STIM}, T_{PW} and T_{IP}). Moreover, minimal undershoot/overshoot is observed in the stimulation current (over the entire range of I_{STIM}) due to careful design of the switching scheme in the DAC, stimulator output stage and the H-bridge. The measured residual charge is ~400 pC for I_{STIM} = 22 µA, and 2.5 nC for I_{STIM} = 5 mA; this results in worst-case residual voltages of 4 mV and 25 mV, respectively, on the 100 nF electrode model, which are well below the safety window of ±100 mV [19].

For *in vitro* validation of optical stimulation, the blue LED was driven by the implant IC with the setup of Fig. 12. Resulting optical stimulation patterns, showing optical intensities of 1.4 mW/mm^2 and ~23 mW/mm^2 for different pulse-widths, are presented in Fig. 16. These were determined based on a measurement of the current waveform through the LED and the characterization result of Fig. 10 (c).

B. Fully Integrated Implant Measurements

In order to verify end-to-end system performance, all components of the implant are integrated into a mm-sized package using flexible polyimide as the substrate and PDMS for encapsulation. The implant (Fig. 17 (c)), has dimensions of 2 mm × 3 mm × 6.5 mm (39 mm^3) and weighs 78 mg. The position of the electrodes and the LED as shown in Fig. 17 (c) is based on simplicity of implant assembly. A more complex electrical/optical neural interface could be designed depending on the requirements of a particular application. It is to be noted that, although we have used biocompatible materials for the major components of our implant (e.g. $BaTiO_3$, polyimide, PDMS and platinum), chronic implantation will require further packaging optimizations such as multilayer encapsulation with parylene [70], [71], or the use of other biomedical grade encapsulants [70], which are beyond the scope of the current work.

Fig. 17 (e) summarizes all performance metrics of the fully integrated implant measured through 10.5 cm of castor oil, and with access only to the electrode/LED terminals for characterization of the stimulation parameter range, as shown

TABLE I
COMPARISON WITH STATE-OF-THE-ART PROGRAMMABLE NEURAL STIMULATION IMPLANTS

Programmable neural stimulation implants	**This work**	[15]	[16]	[17]	[18], [19]	[20], [21]
Process technology	**0.18 µm HV**	0.35 µm	N/A	0.18 µm HV	0.35 µm	3 µm
Wireless powering method	**Ultrasound**	Ultrasound	Resonant RF cavity	Inductive	Inductive	Inductive
Stimulation modality	**Electrical/Optical**[a]	Electrical	Optical	Electrical	Electrical/Optical	Electrical
No. of stim. channels	**4**	1	1	160	4 (active) + 4 (return)	1
Max. supply voltage for electrical stim. (V)	**15**	3.3	N/A	± 12	± 2.1	17
Stimulation current (µA) / resolution	**22 – 5,000 / 8 bits**	0 – 640 / 5 bits	N/A	Up to 500 / 7 bits	12 – 1,500 / 5 bits	200 – 30,000 / (res. not available)
Pulse-width (µs) / resolution	**14 – 470 / 5 bits**	200 (fixed) / N/A	100 – 10,000 / N/A	Up to 8,000 / <10 bits[e]	16 – 512 / 5 bits	4 – 512 / 8 bits
Max. optical intensity (mW/mm^2)	**23**	N/A	40	N/A	17.5	N/A
Custom external TX designed?	**No**	Not reported	Yes	Yes	Yes	Yes
Implant fully integrated?	**Yes**	Yes	Yes	Yes	No	Yes
Implant volume (mm^3)	**39**	1,020[b]	25[c]	500	–	50.3
Tissue depth (cm)	**10.5**	5	< 0.5[d]	< 0.5[d]	1	Not reported
Depth/volume FOM (mm^{-2})	**2.7**	0.05	< 0.2	< 0.01	–	–

[a] *In vivo* demonstration of optogenetic stimulation is a part of future work.
[b] Not including volume of the rechargeable battery.
[c] Volume of their peripheral nerve stimulator.
[d] Estimated from implant location under the skin of a rodent (large tissue depth likely not a major requirement for rodents).
[e] Bits estimated from reported resolution and pulse width.

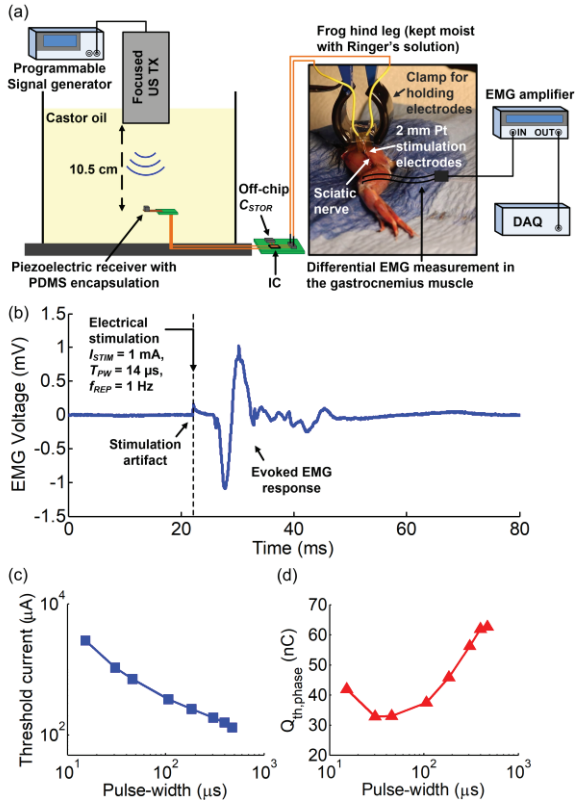

Fig. 18. (a) Experimental setup for frog sciatic nerve stimulation and EMG recording, (b) measured EMG response, and measured strength-duration (S-D) relationships showing: (c) threshold current and (d) threshold charge per phase ($Q_{th,phase}$).

in the measurement setup of Fig. 17 (a). We have also performed a similar test through 6 cm of porcine tissue (attenuation of ~0.8 dB/cm/MHz [34]), as shown in Fig. 17 (b), demonstrating successful operation at a large depth in a tissue environment. The depth for this demonstration was limited by our setup for stacking meat slices. An example stimulation current waveform for this measurement is shown in Fig. 17 (c).

C. Sciatic Nerve Electrical Stimulation Experiments

To further validate functionality, *in vivo* electrical stimulation experiments, along with electromyogram (EMG) recording, were performed in humanely euthanized African clawed frogs (*Xenopus laevis*) under a research protocol approved by the Institutional Animal Care and Use Committee (IACUC). The experimental setup (Fig. 18 (a)) allowed modeling of a large wireless powering depth, while demonstrating sciatic nerve stimulation in a small animal, and accurately quantifying *in vivo* response. EMG signals were recorded in the gastrocnemius (GM) muscle of the frog hind leg using a frontend amplifier (Model 3000, A-M Systems) and a data acquisition unit (PXI-5105, National Instruments). The signals were amplified (500×), filtered (1 Hz – 3 kHz), and sampled at 100 kHz.

Through this experiment, we successfully observed that the magnitude and frequency of twitching response in the GM muscle was in agreement with our stimulation parameters. Fig 18 (b) shows a measurement of the evoked EMG response due to stimulation of the sciatic nerve with I_{STIM} = 1 mA, T_{PW} = 14 µs, and f_{REP} = 1 Hz. In order to further quantify the excitability of the frog sciatic nerve with our stimulator, a strength-duration (S-D) relationship was evaluated, as shown in Fig. 18 (c) and (d). These plots were obtained by measuring the minimum I_{STIM} (threshold), for a fixed T_{PW}, required for a visual onset of twitching response in the GM muscle. Threshold I_{STIM} and threshold charge per phase ($Q_{th,phase}$) closely match well-known S-D curves for biphasic current-controlled stimulation pulses [39], [40], thus, demonstrating the feasibility and efficacy of our fully programmable stimulator.

D. Performance Summary and Comparison

Table I benchmarks the performance of the overall implant system with state-of-the-art stimulators. Due to ultrasonic power delivery, and careful co-design of the piezo and the power recovery circuit, this implant can operate at a depth of

10.5 cm in a tissue phantom (castor oil). Our achieved depth/volume FOM is >10× better than other IC-based programmable neural stimulators. Compared to [15] which also uses ultrasonic powering, our implant has a 26× lower volume, a 54× higher FOM, and a 4.5× higher maximum stimulator supply voltage. In addition, we have demonstrated a data DL with low MD (3%) and BER ($<10^{-5}$), high compliance voltage (15 V), and a wide range of stimulation parameters sufficient for various PNS applications. While other state-of-the-art stimulators based on resonant RF cavity or inductive power transfer have also demonstrated external TX designs (in addition to the implants) for optimizing the end-to-end link PTE, custom TX design was not a focus of this work.

VIII. Conclusion

An electrical stimulation implant is demonstrated with >10× improvement in the depth/volume ratio over existing IC-based neurostimulators. The fully integrated implant measures just 2 mm × 3 mm × 6.5 mm (39 mm^3, 78 mg), and operates at a large depth of 10.5 cm in a tissue phantom. This significant improvement was enabled by the use of ultrasound for wireless powering (at safe intensity levels 3× below the FDA limit), and a unique co-design strategy for complete operation of the implant during the charging transient of C_{STOR}. The implant system also implements a robust DL command/data transfer protocol for fully programmable stimulation, and a high compliance voltage (15 V) stimulator for chronic applications. The stimulator supports biphasic current-controlled stimulation with a wide range of parameters required for electrical stimulation of peripheral nerves. The implant also includes a blue LED which could enable optogenetic stimulation applications in the future. The capability of the implant is demonstrated through *in vitro* characterizations, and electrical stimulation experiments of a sciatic nerve, enabling its use for next-generation electroceuticals. Future work involves design of a conformal ultrasound TX array for optimization of the end-to-end ultrasonic link efficiency, investigating techniques to mitigate the effect of implant misalignment, and biocompatible packaging of the implant for chronic *in vivo* applications.

Acknowledgment

The authors thank Prof. Khuri-Yakub and Prof. Creasey at Stanford University for their insight and valuable discussions. We also acknowledge Mentor Graphics for the use of Analog FastSPICE (AFS) Platform.

References

[1] K. Famm, B. Litt, K. J. Tracey, E. S. Boyden, and M. Slaoui, "A jump-start for electroceuticals," *Nature*, vol. 496, pp. 159–161, Apr. 2013.

[2] E. Waltz, "A spark at the periphery," *Nat. Biotechnol.*, vol. 34, no. 9, pp. 904–908, Sep. 2016.

[3] B. Bonaz, C. Picq, V. Sinniger, J. F. Mayol, and D. Clarencon, "Vagus nerve stimulation: from epilepsy to the cholinergic anti-inflammatory pathway," *Neurogastroenterol. Motil.*, vol. 25, no. 3, pp. 208–221, Mar. 2013.

[4] J. W. Lee, D. Kim, S. Yoo, H. Lee, G.-H. Lee, and Y. Nam, "Emerging neural stimulation technologies for bladder dysfunctions," *Int. Neurourol. J.*, vol. 19, no. 1, pp. 3–11, Mar. 2015.

[5] G. H. Creasey and M. D. Craggs, *Functional electrical stimulation for bladder, bowel, and sexual function*, 1st ed., vol. 109. Elsevier B.V., 2012.

[6] M. Brinton, J. L. Chung, A. Kossler, K. H. Kook, J. Loudin, M. Franke, and D. Palanker, "Electronic enhancement of tear secretion," *J. Neural Eng.*, vol. 13, no. 1, pp. 1–8, Feb. 2016.

[7] X. Li, W. A. Serdijn, W. Zheng, Y. Tian, and B. Zhang, "The injectable neurostimulator: an emerging therapeutic device," *Trends Biotechnol.*, vol. 33, no. 7, pp. 388–394, Jul. 2015.

[8] J. H. Schulman, "The feasible FES system: Battery powered BION stimulator," *Proc. IEEE*, vol. 96, no. 7, pp. 1226–1239, Jul. 2008.

[9] T. J. Foutz, D. M. Ackermann, K. L. Kilgore, and C. C. McIntyre, "Energy efficient neural stimulation: coupling circuit design and membrane biophysics," *PLoS One*, vol. 7, no. 12, pp. 1–8, Dec. 2012.

[10] Y. Shih, T. Shen, and B. Otis, "A 2.3 µW wireless intraocular pressure/temperature monitor," *IEEE J. Solid-State Circuits*, vol. 46, no. 11, pp. 2592–2601, Nov. 2011.

[11] S. Majerus, I. Makovey, H. Zhui, W. Ko, and M. S. Damaser, "Wireless implantable pressure monitor for conditional bladder neuromodulation," in *2015 IEEE Biomed. Circuits Syst. Conf.*, Oct. 2015, pp. 1–4.

[12] R. Muller *et al.*, "A minimally invasive 64-channel wireless µECoG implant," *IEEE J. Solid-State Circuits*, vol. 50, no. 1, pp. 344–359, Jan. 2015.

[13] A. Yakovlev, J. Jang, D. Pivonka, and A. Poon, "A 11 µW sub-pJ/bit reconfigurable transceiver for mm-sized wireless implants," in *Proc. IEEE 2013 Cust. Integr. Circuits Conf.*, Sep. 2013, pp. 1–4.

[14] D. Seo *et al.*, "Wireless recording in the peripheral nervous system with ultrasonic neural dust," *Neuron*, vol. 91, no. 3, pp. 529–539, Aug. 2016.

[15] Y.-S. Luo *et al.*, "Ultrasonic power/data telemetry and neural stimulator with OOK-PM signaling," *IEEE Trans. Circuits Syst. II*, vol. 60, no. 12, pp. 827–831, Dec. 2013.

[16] K. L. Montgomery *et al.*, "Wirelessly powered, fully internal optogenetics for brain, spinal and peripheral circuits in mice," *Nat. Methods*, vol. 12, no. 10, pp. 969–974, Oct. 2015.

[17] Y.-K. Lo *et al.*, "A 176-channel 0.5cm^3 0.7g wireless implant for motor function recovery after spinal cord injury," in *Proc. IEEE Int. Solid-State Circuits Conf.*, Feb. 2016, pp. 382–384.

[18] H.-M. Lee and M. Ghovanloo, "A power-efficient wireless capacitor charging system through an inductive link," *IEEE Trans. Circuits Syst. II*, vol. 60, no. 10, pp. 707–711, Oct. 2013.

[19] H.-M. Lee, K. Y. Kwon, W. Li, and M. Ghovanloo, "A power-efficient switched-capacitor stimulating system for electrical/optical deep brain stimulation," *IEEE J. Solid-State Circuits*, vol. 50, no. 1, pp. 360–374, Jan. 2015.

[20] G. E. Loeb, C. J. Zamin, J. H. Schulman, and P. R. Troyk, "Injectable microstimulator for functional electrical stimulation," *Med. Biol. Eng. Comput.*, vol. 29, pp. 13–19, Feb. 1991.

[21] M. J. Kane, P. P. Breen, F. Quondamatteo, and G. ÓLaighin, "BION microstimulators: a case study in the engineering of an electronic implantable medical device.," *Med. Eng. Phys.*, vol. 33, no. 1, pp. 7–16, Jan. 2011.

[22] P. J. Larson and B. C. Towe, "Miniature ultrasonically powered wireless nerve cuff stimulator," in *2011 5th Int. IEEE/EMBS Conf. Neural Eng.*, Apr. 2011, pp. 265–268.

[23] M. J. Weber, A. Bhat, T. C. Chang, J. Charthad, and A. Arbabian, "A miniaturized ultrasonically powered programmable optogenetic implant stimulator system," in *Proc. IEEE Topical Conf. Biomed. Wireless Technol., Netw., Sens. Syst.*, Jan. 2016, pp. 12–14.

[24] G. Shin, *et al.*, "Flexible near-field wireless optoelectronics as subdermal implants for broad applications in optogenetics," *Neuron*, vol. 93, no. 3, pp. 1–13, Feb. 2017.

[25] J. S. Ho *et al.*, "Wireless power transfer to deep-tissue microimplants," *Proc. Natl. Acad. Sci. U. S. A.*, vol. 111, no. 22, pp. 7974–9, Jun. 2014.

[26] S. T. Lee, P. A. Williams, C. E. Braine, D. Lin, S. W. M. John, and P. P. Irazoqui, "A miniature, fiber-coupled, wireless, deep-brain optogenetic stimulator," *IEEE Trans. Neural Syst. Rehabil. Eng.*, vol. 23, no. 4, pp. 655–664, Jul. 2015.

[27] J. Charthad, M. J. Weber, T. C. Chang, and A. Arbabian, "A mm-sized implantable medical device (IMD) with ultrasonic power transfer and a hybrid bi-directional data link," *IEEE J. Solid-State Circuits*, vol. 50, no. 8, pp. 1741–1753, Aug. 2015.

[28] F. Mazzilli, C. Lafon, and C. Dehollain, "A 10.5 cm ultrasound link for deep implanted medical devices," *IEEE Trans. Biomed. Circuits Syst.*, vol. 8, no. 5, pp. 738–750, Oct. 2014.

[29] T. C. Chang, M. L. Wang, J. Charthad, M. J. Weber, and A. Arbabian, "A 30.5 mm^3 fully packaged implantable device with duplex ultrasonic data

and power links achieving 95kb/s with <10^{-4} BER at 8.5 cm depth," in *Proc. IEEE Int. Solid-State Circuits Conf.*, Feb. 2017, pp. 460–461.
[30] J. W. Hand, A. Shaw, N. Sadhoo, S. Rajagopal, R. J. Dickinson, and L. R. Gavrilov, "A random phased array device for delivery of high intensity focused ultrasound," *Phys. Med. Biol.*, vol. 54, no. 19, pp. 5675–5693, Oct. 2009.
[31] P. Gelat, G. Ter Haar, and N. Saffari, "The optimization of acoustic fields for ablative therapies of tumours in the upper abdomen," *Phys. Med. Biol.*, vol. 57, no. 24, pp. 8471–8497, Dec. 2012.
[32] M. Meng and M. Kiani, "Design and optimization of ultrasonic wireless power transmission links for millimeter-sized biomedical implants," *IEEE Trans. Biomed. Circuits Syst.*, vol. 11, no. 1, pp. 98–107, Feb. 2017.
[33] T. C. Chang, M. J. Weber, M. L. Wang, J. Charthad, B. T. Khuri-Yakub, and A. Arbabian, "Design of tunable ultrasonic receivers for efficient powering of implantable medical devices with reconfigurable power loads," *IEEE Trans. Ultrason. Ferroelectr. Freq. Control*, vol. 63, no. 10, pp. 1554–1562, Oct. 2016.
[34] S. A. Goss, R. L. Johnston, and F. Dunn, "Comprehensive compilation of empirical ultrasonic properties of mammalian tissues," *J. Acoust. Soc. Am.*, vol. 64, no. 2, pp. 423–57, Aug. 1978.
[35] D. D. Zhou and E. Greenbaum, *Implantable Neural Prostheses 2 Techniques and Engineering Approaches*. New York, NY: Springer US, 2009.
[36] C. Towne, K. L. Montgomery, S. M. Iyer, K. Deisseroth, and S. L. Delp, "Optogenetic control of targeted peripheral axons in freely moving animals," *PLoS One*, vol. 8, no. 8, pp. 1–10, Aug. 2013.
[37] C. M. Gregory and C. S. Bickel, "Recruitment patterns in human skeletal muscle during electrical stimulation," *Phys. Ther.*, vol. 85, no. 4, pp. 358–364, Apr. 2005.
[38] P. H. Gorman and J. T. Mortimer, "The effect of stimulus parameters on the recruitment characteristics of direct nerve stimulation," *IEEE Trans. Biomed. Eng.*, vol. 30, no. 7, pp. 407–414, Jul. 1983.
[39] L. A. Geddes and J. D. Bourland, "The strength-duration curve," *IEEE Trans. Biomed. Eng.*, vol. BME-32, no. 6, pp. 458–459, Jun. 1985.
[40] J. P. Reilly, *Applied Bioelectricity: From Electrical Stimulation to Electropathology*. 1998.
[41] A. E. Snellings and W. M. Grill, "Effects of stimulation site and stimulation parameters on bladder inhibition by electrical nerve stimulation," *BJU Int.*, vol. 110, no. 1, pp. 136–143, Jul. 2012.
[42] M. E. Llewellyn, K. R. Thompson, K. Deisseroth, and S. L. Delp, "Orderly recruitment of motor units under optical control in vivo," *Nat. Med.*, vol. 16, no. 10, pp. 1161–1165, Sep. 2010.
[43] W. Ngamkham, M. N. Van Dongen, and W. A. Serdijn, "Biphasic stimulator circuit for a wide range of electrode-tissue impedance dedicated to cochlear implants," in *Proc. IEEE Int. Symp. Circuits and Syst.*, May 2012, pp. 1083–1086.
[44] W. Biederman *et al.*, "A 4.78 mm^2 fully-integrated neuromodulation SoC combining 64 acquisition channels with digital compression and simultaneous dual stimulation," *IEEE J. Solid-State Circuits*, vol. 50, no. 4, pp. 1038–1047, Apr. 2015.
[45] S. K. Arfin and R. Sarpeshkar, "An energy-efficient, adiabatic electrode stimulator with inductive energy recycling and feedback current regulation," *IEEE Trans. Biomed. Circuits Syst.*, vol. 6, no. 1, pp. 1–14, Feb. 2012.
[46] S. Ha *et al.*, "A 16-channel wireless neural interfacing SoC with RF-powered energy-replenishing adiabatic stimulation," in *2015 IEEE Symp. VLSI Circuits (VLSI) Dig.*, 2015, pp. C106–C107.
[47] J. Lee, H. G. Rhew, D. R. Kipke, and M. P. Flynn, "A 64 channel programmable closed-loop neurostimulator with 8 channel neural amplifier and logarithmic ADC," *IEEE J. Solid-State Circuits*, vol. 45, no. 9, pp. 1935–1945, Sep. 2010.
[48] M. Ortmanns, A. Rocke, M. Gehrke, and H. J. Tiedtke, "A 232-channel epiretinal stimulator ASIC," *IEEE J. Solid-State Circuits*, vol. 42, no. 12, pp. 2946–2959, Dec. 2007.
[49] M. Monge *et al.*, "A fully intraocular high-density self-calibrating epiretinal prosthesis," *IEEE Trans. Biomed. Circuits Syst.*, vol. 7, no. 6, pp. 747–760, Dec. 2013.
[50] M. Yip, R. Jin, H. H. Nakajima, K. M. Stankovic, and A. P. Chandrakasan, "A fully-implantable cochlear implant SoC with piezoelectric middle-ear sensor and arbitrary waveform neural stimulation," *IEEE J. Solid-State Circuits*, vol. 50, no. 1, pp. 214–229, Jan. 2015.
[51] H. Chandrakumar and D. Markovic, "A high dynamic-range neural recording chopper amplifier for simultaneous neural recording and stimulation," *IEEE J. Solid-State Circuits*, vol. 52, no. 3, pp. 645–656, Mar. 2017.
[52] S. Stanslaski *et al.*, "Design and validation of a fully implantable, chronic, closed-loop neuromodulation device with concurrent sensing and stimulation," *IEEE Trans. Neural Syst. Rehabil. Eng.*, vol. 20, no. 4, pp. 410–421, Jul. 2012.
[53] W. Chen *et al.*, "A fully integrated 8-channel closed-loop neural-prosthetic CMOS SoC for real-time epileptic seizure control," *IEEE J. Solid-State Circuits*, vol. 49, no. 1, pp. 232–247, Jan. 2014.
[54] G. Palumbo and D. Pappalardo, "Charge pump circuits: An overview on design strategies and topologies," *IEEE Circuits Syst. Mag.*, vol. 10, no. 1, pp. 31–45, Mar. 2010.
[55] H.-M. Lee and M. Ghovanloo, "An integrated power-efficient active rectifier with offset-controlled high speed comparators for inductively powered applications," *IEEE Trans. Circuits Syst. I, Reg. Papers*, vol. 58, no. 8, pp. 1749–1760, Aug. 2011.
[56] J. P. Ball, B. A. Mound, J. C. Nino, and J. B. Allen, "Biocompatible evaluation of barium titanate foamed ceramic structures for orthopedic applications," *J. Biomed. Mater. Res. - Part A*, vol. 102, no. 7, pp. 2089–2095, Jul. 2014.
[57] A. I. Al-Kalbani, M. R. Yuce, and J. M. Redoute, "Design methodology for maximum power transmission, optimal BER-SNR and data rate in biomedical implants," *IEEE Commun. Lett.*, vol. 17, no. 10, pp. 1897–1900, Oct. 2013.
[58] A. Yakovlev, J. H. Jang, and D. Pivonka, "An 11 μw sub-pJ/bit reconfigurable transceiver for mm-sized wireless implants," *IEEE Trans. Biomed. Circuits Syst.*, vol. 10, no. 1, pp. 175–185, Feb. 2016.
[59] M. Tabesh, N. Dolatsha, A. Arbabian, and A. M. Niknejad, "A power-harvesting pad-less millimeter-sized radio," *IEEE J. Solid-State Circuits*, vol. 50, no. 4, pp. 1–16, Apr. 2015.
[60] E. Greenwald *et al.*, "A CMOS current steering neurostimulation array with integrated DAC calibration and charge balancing," *IEEE Trans. Biomed. Circuits Syst.*, vol. 11, no. 2, pp. 324–335, Apr. 2017.
[61] J. J. Sit and R. Sarpeshkar, "A low-power blocking-capacitor-free charge-balanced electrode-stimulator chip with lesst than 6 nA DC error for 1-mA full-scale stimulation," *IEEE Trans. Biomed. Circuits Syst.*, vol. 1, no. 3, pp. 172–183, Sep. 2007.
[62] S. F. Cogan, "Neural stimulation and recording electrodes," *Annu. Rev. Biomed. Eng.*, vol. 10, pp. 275–309, Aug. 2008.
[63] H. Liske, X. Qian, P. Anikeeva, K. Deisseroth, and S. Delp, "Optical control of neuronal excitation and inhibition using a single opsin protein, ChR2," *Sci. Rep.*, vol. 3, pp. 1–7, Oct. 2013.
[64] T. Zaid, S. Saat, Y. Yusop, and N. Jamal, "Contactless energy transfer using acoustic approach - A review," in *I4CT 2014 - 1st Int. Conf. Comput. Commun. Control Technol. Proc.*, Sep. 2014, pp. 376–381.
[65] M. Liebler, S. Ginter, T. Dreyer, and R. E. Riedlinger, "Full wave modeling of therapeutic ultrasound: efficient time-domain implementation of the frequency power-law attenuation," *J. Acoust. Soc. Am.*, vol. 116, no. 5, pp. 2742–2750, Nov. 2004.
[66] B. E. Treeby, B. T. Cox, E. Z. Zhang, S. K. Patch, and P. C. Beard, "Measurement of broadband temperature-dependent ultrasonic attenuation and dispersion using photoacoustics," *IEEE Trans. Ultrason. Ferroelectr. Freq. Control*, vol. 56, no. 8, pp. 1666–1676, Aug. 2009.
[67] J. A. Jensen, "Medical ultrasound imaging," *Prog. Biophys. Mol. Biol.*, vol. 93, no. 1-3, pp. 153–165, Jan–Apr. 2007.
[68] A. Bhuyan *et al.*, "Integrated circuits for volumetric ultrasound imaging with 2-D CMUT arrays," *IEEE Trans. Biomed. Circuits Syst.*, vol. 7, no. 6, pp. 796–804, Dec. 2013.
[69] M. L. Wang, T. C. Chang, T. Teisberg, M. J. Weber, J. Charthad, and A. Arbabian, "Closed-loop ultrasonic power and communication with multiple miniaturized active implantable medical devices," in *Proc. IEEE Int. Ultrason. Symp.*, Sep. 2017, pp. 1–4.
[70] S. Majerus *et al.*, "Wireless bladder pressure monitor for closed-loop bladder neuromodulation," *Sensors*, pp. 7–9, Nov. 2016.
[71] P. Wang and W. H. Ko, "Non-hermetic micropackage for chronic implantable systems," *Int. Symp. Microelectron.*, Sep. 2013, pp. 1–5.

Jayant Charthad (S'13) received the B.Tech. degree from Indian Institute of Technology, Bombay, India in 2009 and the M.S. degree from Stanford University, CA, USA, in 2013, both in electrical engineering. He is currently a Ph.D. candidate in electrical engineering at Stanford University, USA.

From 2009 to 2011, he was with Texas Instruments, Bangalore, India, where he designed low-dropout regulator ICs. He spent summer 2012 with the SAR ADC team at Linear Technology, Milpitas, CA, USA. His research interests include wireless power transfer, implantable medical devices, bio-sensing, and integrated circuit and system design.

Mr. Charthad was a recipient of the Analog Devices Outstanding Student Designer Award in 2014, the Centennial Teaching Assistant Award in 2015 and the 2015 James F. Gibbons Outstanding Student Teaching Award in Electrical Engineering at Stanford University.

Ting Chia Chang (S'11) received the B.S degree in EECS from UC Berkeley in 2012 and the M.S. degree in EE from Stanford University in 2015. He is currently a Ph.D. candidate in Electrical Engineering at Stanford University.

During his undergraduate study, he worked on nanoelectronic devices and interned in Microelectronic Research Center at UT Austin in the summer of 2011. His current research interests include wireless power delivery, wireless communication, acoustics applications, implantable medical devices, and digital and analog low power integrated circuit design.

Mr. Chang received Honorable Mentions from National Science Foundation Graduate Research Fellowship in 2014, the Analog Device Outstanding Student Design Award in 2017, and the Best Paper Award in IEEE BIOCAS Conference in 2017.

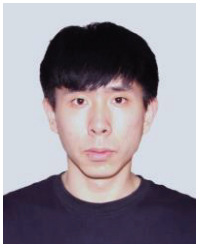

Zhaokai Liu received the B.S degree in microelectronics from the School of Electronics Engineering and Computer Science, Peking University, Beijing, China, in 2017. He is currently a Ph.D. candidate in electrical engineering at University of California, Berkeley.

He spent summer 2016 with Professor Amin Arbabian's research group at Stanford. His research interests include ADC design, implantable medical devices and integrated circuit and system design.

He was a recipient of the National Scholarship Award in 2015 and Merit Student Award in the school of computer science and electrical engineering at Peking University.

Ahmed Sawaby (S'17) received his B.S. degree for Cairo University, Giza, Egypt, in 2014. He then pursued his M.S. degree at the same university through 2017, both in electrical engineering. He is currently pursuing his Ph.D. degree at Stanford University, CA, USA.

From 2014 to 2015, he joined Cairo Circuits and Systems Lab, where he designed high-speed DACs for a frequency hopping transmitter front-end. In 2015 to 2016, he joined Silicon Vision, Egypt, as an RF design engineer where he worked on designing the PMU of Synopsys's state-of-the-art 55nm BLE IP. In 2016 to 2017, he joined the Arbabian Lab at Stanford University as a visiting student where he worked on implantable medical chips.

Mr. Sawaby was a recipient of the Stanford Graduate Fellowship (SGF).

Marcus J. Weber (S'10) received the B.S. degree from the University of Wisconsin-Madison, Madison, WI, USA, in 2012 and the M.S. degree from Stanford University, Stanford, CA, USA, in 2014, both in electrical engineering. He is currently pursuing the Ph.D. degree in electrical engineering at Stanford University.

In 2008, he was a software engineering intern at GE Healthcare. He also worked as an electrical engineer in three cooperative education semesters at NASA Johnson Space Center from 2009 to 2011. From 2010 to 2012 he performed research as an undergraduate student at the University of Wisconsin-Madison investigating the atmospheric effects on terahertz (THz) wave propagation. His research interests are broad and include implantable devices, bio-sensing, wireless power and communication, energy harvesting, low power electronics, and analog and RF circuit design.

Mr. Weber was a recipient of the Stanford Graduate Fellowship (SGF), the National Science Foundation Graduate Research Fellowship (NSF-GRP), the best paper award at the 2016 IEEE Conference on Biomedical Wireless Technologies, Networks, and Sensing Systems, and the Fairchild Semiconductor Student Designer Award.

Sam Baker received the B.A. in Zoology from the University of Cambridge, Cambridge, U.K., in 2008, and the VetMB in Veterinary Medicine from the University of Cambridge, Cambridge, U.K., in 2011.

In 2011, he began a residency in Laboratory Animal Medicine at Columbia University, NY, USA, becoming a Diplomate of the American College of Laboratory Animal Medicine in 2014. From 2014-2016 he worked as a Clinical Veterinarian in the Institute of Comparative Medicine at Columbia University, NY, USA. He is currently a Staff Veterinarian in the Veterinary Service

Center at Stanford University, CA, USA. He specializes in the perioperative care of laboratory animals, working with researchers to develop and refine animal research models.

Felicity Gore received the B.A. in natural sciences from the University of Cambridge, Cambridge, U.K., in 2009 and the Ph.D. in neurobiology and behavior from Columbia University, NY, USA, in 2016.

From 2008-2009, she was a Research Assistant in the Department of Psychology at the University of Cambridge. She is currently a postdoctoral fellow in the Department of Bioengineering at Stanford University, CA, USA. Her research interests include the development and application of optical techniques to examine the neural circuits that mediate motivated behaviors.

Dr. Gore's awards and honors include the Stanford School of Medicine Dean's Postdoctoral Fellowship, and the Walter V. and Idun Berry Postdoctoral Fellowship.

Stephen A. Felt, DVM, MPH, DACVPM, DACLAM, received his veterinary degree from University of Wisconsin School of Veterinary Medicine and completed his public health education at the Uniformed Services University, Bethesda, Maryland.

He is currently an Associate Professor in the Department of Comparative Medicine at Stanford University School of Medicine. He conducted his residency training in laboratory animal medicine at the Walter Reed Army Institute of Research (WRAIR). Prior to arriving at Stanford, Dr. Felt served as the Director for the Animal Resources Program at the Naval Medical Research Unit No. 3 in Cairo, Egypt. His research interest focuses on infectious diseases, particularly zoonoses, and developing translational animal models.

Dr. Felt has successfully led and worked collaboratively on funded research projects, including NIH R25, R21 and R01 grants. Honors for research include First Place Vice President's Resident Research Award, Triological Society (2013) and for teaching include Stanford University Great Teaching Showcase Awardee (2018).

Amin Arbabian (S'06–M'12) received the Ph.D. degree in electrical engineering and computer science from the University of California at Berkeley (UC Berkeley), Berkeley, CA, USA, in 2011.

From 2007 and to 2008, he was part of the Initial Engineering Team, Tagarray, Inc., Palo Alto, CA, USA. He was with the Qualcomm's Corporate Research and Development Division, San Diego, CA, USA, in 2010, where he designed circuits for next-generation ultra-low power wireless transceivers. In 2012, he joined Stanford University, Stanford, CA, USA, as an Assistant Professor of electrical engineering, where he is currently a Frederick E. Terman Fellow with School of Engineering. His current research interests include high-frequency systems, medical imaging, Internet-of-Everything devices including wireless power delivery techniques, and medical implants.

Dr. Arbabian was a recipient or co-recipient of the 2016 Stanford University Tau Beta Pi Award for Excellence in Undergraduate Teaching, the 2015 NSF CAREER Award, the 2014 DARPA Young Faculty Award including the Director's Fellowship in 2016, the 2013 Hellman Faculty Scholarship, the 2010–2011, 2014–2015, and 2016–2017 Qualcomm Innovation fellowships, and best paper awards at the 2017 IEEE Biomedical Circuits and Systems Conference, the 2016 IEEE Conference on Biomedical Wireless Technologies, Networks, and Sensing Systems, 2014 IEEE VLSI Circuits symposium, 2013 IEEE International Conference on Ultra-Wideband (ICUWB), the 2010 IEEE Jack Kilby Award for Outstanding Student Paper at the International Solid-State Circuits Conference, and two time second place best student paper awards at 2008 and 2011 RFIC symposiums. He currently serves on the steering committee of RFIC Symposium, the technical program committees of RFIC symposium, ESSCIRC, and VLSI Circuits Symposium, and as an Associate Editor of the IEEE SOLID-STATE CIRCUITS LETTERS and the IEEE JOURNAL OF ELECTROMAGNETICS, RF AND MICROWAVES IN MEDICINE AND BIOLOGY.